Acta Oceanol. Sin., 2021, Vol. 40, No. 3, P. 134–141
https://doi.org/10.1007/s13131-021-1708-3
http://www.hyxb.org.cn
E-mail: hyxbe@263.net

Measuring solar irradiance profiles in the Arctic sea ice using fiber optic spectrometry via inclined holes

Zexia Qiu[1], Hangzhou Wang[1]*, Tao Li[2], Hong Song[1], Yuanqian Wu[3], Tingting Yan[3], Ying Chen[1]

[1] Ocean College, Zhejiang University, Zhoushan 316021, China

[2] Key Laboratory of Physical Oceanography, Ocean University of China, Qingdao 266100, China

[3] Zhejiang Heli Electrical Engineering Co., Ltd., Taizhou 317000, China

Received 19 November 2019; accepted 25 April 2020

© Chinese Society for Oceanography and Springer-Verlag GmbH Germany, part of Springer Nature 2021

Abstract

An irradiance profile measurement approach and profiling system were developed to measure the solar irradiance profile of the Arctic sea ice using fiber optic spectrometry. The approach involved using a miniature spectrometer to sense light signals collected and transmitted from a fiber probe. The fiber probe was small, and could thus move freely in inclined bore holes drilled in sea ice with its optical entrance pointing upward. The input-output relationship of the system was analyzed and built. Influence factors that determined the system output were analyzed. A correctional system output approach was proposed to correct the influence of these factors, and to obtain the solar irradiance profile based on the measurements outputted by this system. The overall performance of the system was examined in two ice floes in the Arctic during the 9th Chinese National Arctic Research Expedition. The measured solar irradiance profiles were in good agreement with those obtained using other commercially available oceanographic radiometers. The derived apparent optical properties of sea ice were comparable to those of similar sea ice measured by other optical instruments.

Key words: solar irradiance, profile, sea ice, fiber optic spectrometry, inclined hole

Citation: Qiu Zexia, Wang Hangzhou, Li Tao, Song Hong, Wu Yuanqian, Yan Tingting, Chen Ying. 2021. Measuring solar irradiance profiles in the Arctic sea ice using fiber optic spectrometry via inclined holes. Acta Oceanologica Sinica, 40(3): 134–141, doi: 10.1007/s13131-021-1708-3

1 Introduction

Sea ice is a kind of translucent material with an intricate internal structure, which is considerably affected by the complicated interaction between physical, biological, and chemical processes in the polar environments (Thomas and Dieckmann, 2009). The enormous area in both polar regions (about 4% of the total surface of the earth) makes sea ice play a significant role in determining global biogeochemical cycles and global climatology via regulating the material and energy exchanges between the ocean and atmosphere (Arrigo, 2014; Vancoppenolle et al., 2013). However, numerous studies indicate that sea ice in the Arctic has been undergoing tremendous changes for the past several decades. These are manifested as trends such as the shrinking of sea ice cover, the reduction in the ice thickness, the declining ice concentration (Arrigo et al., 2008; Maslanik et al., 2007; Serreze et al., 2007). These variations reflect the combined influence of thermodynamic and dynamic processes in the Arctic Ocean, among which solar radiation is of key importance.

Solar radiation (especially the shortwave radiation) has a significant role in governing the heat- and mass-balance of sea ice (Grenfell et al., 2006; Leu et al., 2015; Nicolaus et al., 2010a). Detailed knowledge about the partitioning of solar radiation in the environment created by sea ice helps understand not only the range of energy absorbed by the snow and sea ice and transmitted to the underlying ocean, but also its formation and decay characteristics and mechanisms. Moreover, the availability of solar radiation is vital for determining the biomass and taxonomic composition of the ice algae communities developed on the snow or ice's surface, in the interior and bottom of ice, and in the upper ocean (Haas et al., 2001; Saenz and Arrigo, 2012). Therefore, solar radiation partitioning is one of the most fundamental concerns in the Arctic sea environment. Until now, the measurements of solar radiation in the Arctic sea environment predominantly focused on the solar radiation above sea ice, which could be used to indicate the fraction of solar radiation incident on, and reflected by, the ice surface separately (Feister and Grewe, 1995; Grenfell and Perovich, 1984). In contrast, there are also some studies measuring solar radiation below ice, from which the part of the solar radiation transmitted to the underlying ocean could be derived (Frey et al., 2011; Nicolaus et al., 2010a; Zhao and Li, 2009). However, knowledge about the distribution of solar radiation at different depths of sea ice, which could be used to indicate the partitioning of solar radiation in sea ice, is rather limited (Ehn et al., 2008b; Light et al., 2008; Light et al., 2015).

Grenfell and Maykut (1977) measured solar irradiance at multiple depths of sea ice by using a fiber-optics light guide to sequentially collect and transmit the light signals at multiple horizontal holes, and then using a portable spectrophotometer to

Foundation item: The National Natural Science Foundation of China under contract No. 41976218; the Joint Zhoushan City and Zhejiang University Cooperation Project under contract No. 2019C81034; the National Key Research and Development Program of China under contract No. 2016YFC1400303; the Program for Zhejiang Leading Team of S&T Innovation under contract No. 2010R50036.

*Corresponding author, E-mail: hangzhouwang@zju.edu.cn

sense them. The holes were drilled at different depths in the wall of a narrow trench that was excavated in ice in advance. Arrigo et al. (1991) obtained the PAR (photosynthetically active radiation) profile within sea ice in a similar manner. The disadvantage of these methods is that the amount and the position of the solar irradiance measured in sea ice are limited by the holes drilled. Light et al. (2008b), Ehn et al. (2008b) and Xu et al. (2012) used a spectrophotometer or spectrometer to measure the radiation signals recorded by a fiber probe that was gradually lowered down to a vertical bore hole with a certain number of increments. Incident radiation variation was measured for the correction of light field variations during each radiation profile measurement. To minimize the influence of the vertical bore hole on the measured irradiance, the fiber probe was specially designed to block the light signal coming directly down the bore hole. However, such a design also results in the solar radiation within a certain zenith angle (e.g., ~15°) being blocked, which might lead to an underestimation of the solar irradiance. Ehn et al. (2008a) gradually drilled an auger hole upward from the bottom of the ice and fed a cosine receptor to the top of the hole to guide the solar radiation signal that was then detected by a spectroradiometer. An irradiance profile was obtained as the hole was gradually drilled with an interval of 0.05 m. Even though the irradiance profile was very accurate, the measurement process was both labor intensive and low in efficiency.

In this study, a novel approach was developed to take *in-situ* measurements of the solar irradiance profile within sea ice based on the fiber optic spectrometry technology via inclined holes instead of vertical ones. First, the general measurement principle and the corresponding profiling system was introduced. Next, we modeled the system signal output to bridge it with the incident light level and developed a correctional approach to get the solar irradiance based on the system output. Finally, the overall measurement performance of the system was examined and evaluated in the Arctic sea environment.

2 Methods

2.1 *Measurement principle*

Special precautions need to be taken while measuring the solar irradiance profile in the Arctic sea ice in terms of the collection and measurement of the solar radiation signals. Direct movement of optical sensor or optical probe within the solid sea ice medium is unrealistic. Meanwhile, non-invasive irradiance measurement technology for use in solid sea ice is still under development. Therefore, approaches involving the use of an optical probe that can be moved freely within a bore hole to collect and transmit the solar signals, and the use of an optical sensor (e.g., spectrophotometer or spectrometer) to sense these signals, was adopted in previous studies to obtain solar irradiance profiles in sea ice (Light et al., 2008). The general measurement principle for this study is very similar. However, a much smaller and simpler optical probe (i.e., cosine receptor; compared with that used by Light et al. (2008) and Ehn et al. (2008b)) was used. This probe could be placed in the bore hole with its upper face (i.e., optical entrance) directly pointing upward to collect the downwelling irradiance signal. To minimize the influence of the bore hole on the collected solar radiation signals, an inclined hole was drilled to keep most of the light field the optical probe faced undisturbed. Compared with the previous approaches mentioned above this configuration can significantly minimize self-blocking of the optical probe, and the uncertainty of the measured solar irradiance could be reduced.

2.2 *System description and measurement considerations*

In this study, a miniature spectrometer (C11009MA, Hamamatsu Photonics K K, Japan) was adopted to measure the solar signal guided by an optical probe (Fig. 1). The spectrometer is a compact module with relevant optical parts and driver electronics sealed inside a metal case. This configuration can effectively overcome the influence of the potential condensation of airborne water when the ambient temperature is lower than the dew point. Moreover, there are no moving parts involved in this module, guaranteeing the reliability and repeatability of the spectrometer. These characteristics are the primary motivations for using this spectrometer module in the harsh Arctic sea environment (e.g., low temperature, high humidity). The module has a spectral range of 340–780 nm and spectral resolution of 9 nm. The specified operating temperature range is 5–40°C. However, Wang et al. (2017) have shown that this module can work normally even at temperatures down to –50°C. A high-transmission silica fiber (Optran® Ultra HWF, CeramOptec®, Germany) was used to transmit the light collected by an optical probe. The fiber has a spectral range of 350–2 200 nm, which covers the spectral bands of the solar radiation of interest (i.e., 350–750 nm). The typical transmission of the fiber is higher than 99%/m and 90%/m for wavelengths approximately longer and shorter than 450 nm, respectively. For the 3.5 m fiber length adopted in this system, at least 96% of the energy of the collected solar signal could be transmitted to the spectrometer for most of wavelengths. This high transmittance is vital for improving the measurement sensitivity of the system and detecting the low solar radiation signal beneath sea ice. A cosine-corrected irradiance probe (CC-3, Ocean Optics, Inc., USA) was connected to one end of the silica fiber via a SMA-905 interface to collect the solar irradiance signal from the Arctic sea environment. It has a spectral range of 350–1 000 nm and has a good cosine response for angles smaller than approximately 78°. The small geometry of the probe (i.e., 6.35 mm in diameter) helps minimize the diameter of the bore hole drilled in sea ice and eventually alleviate the influence of the bore hole on the light field of sea ice. To increase signal coupling between the spectrometer and the optical fiber, a fiber collimating lens (SPL-COL-5, SPL-tech, China) was placed (i.e., attached at the optical entrance of the spectrometer) between the spectrometer and the other end of the fiber. Other than the fiber probe exposed to the Arctic sea environment, all other parts of the system (i.e., the spectrometer and relevant driver electronics, lens, and part of the fiber) were fixed within a waterproof case for protection.

To obtain the solar irradiance profile within sea ice first an inclined auger hole was drilled, which had a diameter of 5 cm

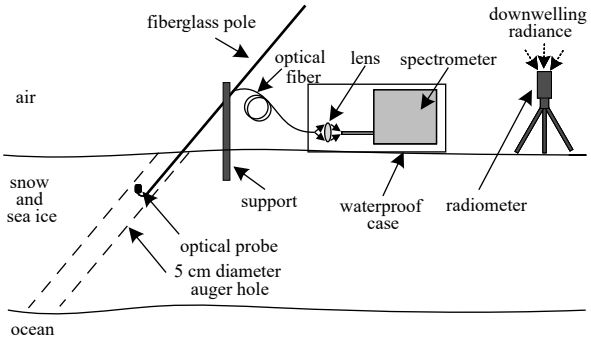

Fig. 1. Schematic diagram of measurement site, including measurements of radiation above and within ice.

and tilt angle of 45° (Fig. 1). We next fixed the optical probe to a fiberglass pole and carefully adjusted the angle between the optical probe and the pole to keep the opaline glass window of the probe pointing upward within the bore hole. The measurement started at the ice surface and ended when the entire length of the fiber (i.e., 3.5 m) was utilized. An irradiance profile was obtained by gradually lowering the optical probe into the auger hole with distance intervals of 10 cm (along the axis direction of the auger hole) to collect the solar irradiance signal, while using the C11009MA miniature spectrometer to sense the signal. Dark outputs were also acquired from the spectrometer for the subsequent correction at the end of the profile measurement by placing the optical probe inside a dark box and taking measurements. Potential intensity fluctuations of the incident solar radiation were monitored during the entire profile measurement using a radiometrically calibrated hyperspectral irradiance sensor (RAMSES-ACC-VIS, TriOS Mess- und Datentechnik GmbH, Germany), which was deployed approximately 1.2 m above the ice surface using a tripod. This radiometer was used broadly in the Arctic sea environment to measure solar irradiance above the ice surface and in the underlying ocean (Lei et al., 2012; Nicolaus et al., 2010b). It has a spectral range of 320–980 nm and spectral accuracy of 0.3 nm. It is worth mentioning that a simultaneous comparison measurement between our system and the radiometer was carried out in air before each profile measurement for the spectral sensitivity correction of our system. This was achieved by placing the optical probe of our system and optical entrance of the radiometer side by side and measuring the downwelling irradiance.

2.3 *System output modeling*

As determined by the optical and electrical characteristics of the spectrometer adopted, the output of the spectrometer is composed of two parts of signal output generated by the incident light signal and the dark output, which is the spectrometer output in the absence of any light and has no relationship with the incident light signal (Wang et al., 2015). This analog spectrometer output is then digitized by an analog-to-digital (AD) circuit involved in the spectrometer driver electronics, hence, the output is generated as AD counts. However, what we want to obtain from the system is the spectral intensity of the solar irradiance. As a result, the relationship between the spectrometer signal output (i.e., the profiling system output) and the spectral intensity of the incident solar irradiance is investigated and modeled in this part, which lays a solid theoretical foundation for the subsequent system output correction.

As mentioned above, the profiling system has a single spectrometer to sense the signal from the fiber probe. The incident light signal E_I goes through several steps from entering the system to becoming the final system output C_s (Fig. 2). First, it is collected and transmitted by the fiber probe and focused at the optical entrance of the spectrometer by a lens. Second, it enters the spectrometer through a slit and is dispersed and re-focused to an internal complementary metal-oxide-semiconductor (CMOS) photodiode array image sensor where each photodiode (i.e., each pixel of the spectrometer) receives a fixed narrow spectral band of photons and converts them into charges. Third, the charges accumulated at each photodiode are sequentially outputted and proportionally converted to analog voltage signals by a charge-to-voltage converter in the internal driver electronics of the spectrometer, under the timing of the spectrometer driver electronics (Nan et al., 2017). Finally, the voltage signal is proportionally digitalized by the AD conversion circuit utilizing a 16-bit

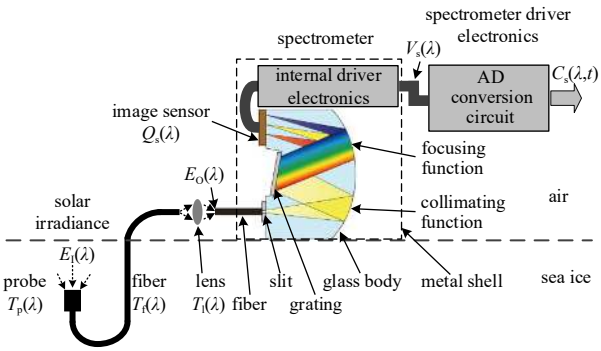

Fig. 2. Schematic of the light signal transmission and conversion, from entering the optical probe to becoming the system output.

AD converter (ADC; AD7988-5, Analog Devices Inc., USA), using a fixed voltage reference (5 V nominal; ADR435B, Analog device Inc., USA).

Based on the above analysis (Fig. 2), the system output $C_s(\lambda)$ at each wavelength λ (i.e., at each photodiode) could be modeled as shown below. For the miniature spectrometer used, the charge $Q_s(\lambda,t)$ accumulated at each wavelength is proportional to the incident light intensity $E_O(\lambda)$ at the spectrometer's optical entrance and the time duration t for the accumulation of the charge (i.e., integration time of the spectrometer). This relationship is given by

$$Q_s(\lambda, t) = k(\lambda)\, E_O(\lambda)\, t, \tag{1}$$

where $k(\lambda)$ is the conversion factor for converting the light intensity entering the spectrometer into photodiode output charge, which is a function of the optical system efficiency, the diffraction efficiency of the grating, and the sensitivity of the image sensor. The wavelength λ is expressed as a fifth order polynomial of pixel of the spectrometer provided by the vendor. And pixel corresponds to the physical position order in which the photodiode sits in the image sensor.

The charge $Q_s(\lambda,t)$ is then converted into voltage signal $V_s(\lambda,t)$ via the internal charge-to-voltage converter of the spectrometer:

$$V_s(\lambda, t) = \varepsilon Q_s(\lambda, t)\,. \tag{2}$$

Further, it is digitized by the 16-bit AD converter with a nominal 5 V voltage reference V_{ref}.

$$\frac{C_s(\lambda, t)}{2^{16}} = \frac{V_s(\lambda, t)}{V_{ref}} \Rightarrow C_s(\lambda, t) = \frac{2^{16}}{V_{ref}} V_s(\lambda, t)\,, \tag{3}$$

where ε is the conversion factor of the charge-to-voltage converter, and $C_s(\lambda,t)$ is the digitized system output. By replacing $Q_s(\lambda,t)$ with Eq. (1) in Eq. (2), and replacing $V_s(\lambda,t)$ with Eq. (2), Eq. (3) can be rewritten as

$$C_s(\lambda, t) = \frac{2^{16}}{V_{ref}} \varepsilon k(\lambda)\, E_O(\lambda)\, t. \tag{4}$$

Equation (4) gives the relationship between the system output C_s and the incident light intensity E_O at the spectrometer's optical entrance. However, intensity of the incident solar irradiance $E_I(\lambda)$

where the fiber probe is placed, which is also the ultimate parameter we want to obtain from the system measurements, has not been included in this equation. Before reaching the optical entrance of the spectrometer, the incident solar irradiance undergoes several processes of being collected, transmitted, and focused by the fiber probe and focusing lens. During these processes, the changes in the spectral intensity of this signal are shown by

$$E_{\mathrm{O}}(\lambda) = E_{\mathrm{I}}(\lambda)\, T_{\mathrm{p}}(\lambda)\, T_{\mathrm{f}}(\lambda)\, T_{\mathrm{l}}(\lambda)\, T_{\mathrm{c}}(\lambda)\,, \tag{5}$$

where $T_{\mathrm{p}}(\lambda)$ is the transmission coefficient of the optical probe, and is primarily determined by the probe's geometric dimension and the material used. $T_{\mathrm{f}}(\lambda)$ is the transmission coefficient of the optical fiber, and is influenced by the material used, core diameter, fiber length, and surface quality of the two ends. $T_{\mathrm{l}}(\lambda)$ is the transmission coefficient of the lens, and $T_{\mathrm{c}}(\lambda)$ is the overall coupling coefficient between the different optical components included (i.e., the probe and the fiber, the fiber and the lens, and the lens and the spectrometer's optical entrance). By replacing $E_{\mathrm{O}}(\lambda)$ with Eq. (5) and rearranging terms, Eq. (4) can be rewritten as

$$\begin{aligned} C_{\mathrm{s}}(\lambda, t) =& \frac{2^{16}}{V_{\mathrm{ref}}} \varepsilon k(\lambda)\, T_{\mathrm{p}}(\lambda)\, T_{\mathrm{f}}(\lambda)\, T_{\mathrm{l}}(\lambda)\, T_{\mathrm{c}}(\lambda)\, E_{\mathrm{I}}(\lambda)\, t \\ =& s(\lambda)\, E_{\mathrm{I}}(\lambda)\, t, \end{aligned} \tag{6}$$

where $s(\lambda) = \dfrac{2^{16}}{V_{\mathrm{ref}}} \varepsilon k(\lambda)\, T_{\mathrm{p}}(\lambda)\, T_{\mathrm{f}}(\lambda)\, T_{\mathrm{l}}(\lambda)\, T_{\mathrm{c}}(\lambda)$ is spectral sensitivity of the combination of the spectrometer, lens, and fiber probe. Equation (6) gives the theoretical model between the system output $C_{\mathrm{s}}(\lambda,t)$ and the incident light level $E_{\mathrm{I}}(\lambda)$, and it denotes that $C_{\mathrm{s}}(\lambda,t)$ is proportional to $E_{\mathrm{I}}(\lambda)$ and integration time t when the spectrometer works at its linear operating range. This relationship agrees well with the fact that more photons will strike the photodiodes and more charges will be generated in the spectrometer accordingly if the incident light intensity is stronger and the integration time is longer. $s(\lambda)$ is strongly wavelength-dependent primarily because of the wavelength dependence of the transmission coefficient of the fiber probe and the lens and the spectral sensitivity of the spectrometer. However, it should be constant at each wavelength λ for a given temperature. Conversely, the spectral intensity of the incident light E_{I} could be calculated via Eq. (6) as

$$E_{\mathrm{I}}(\lambda) = \frac{C_{\mathrm{s}}(\lambda, t)}{s(\lambda)\, t}. \tag{7}$$

2.4 *System output correction*

From the above analysis, we notice that the influences of the dark output of the spectrometer and the spectral sensitivity of the system (i.e., the combination of the spectrometer, lens, and fiber probe) are still in the measured solar irradiance profile. The immersion factor of the cosine receptor and the potential intensity fluctuation of the incident solar irradiance are also involved. The immersion factor is caused by transmissivity variations of the cosine receptor when it is used in different mediums. The spectral sensitivity of the system was calibrated in air using the comparison measurements mentioned in Section 2.2. However, the cosine receptor was inserted in the auger hole (i.e., immersed in water) where its transmissivity would become smaller than that in air. An underestimation of the solar irradiance in ice will happen if the immersion factor is not corrected. Additionally, the irradiance profile measurements are primarily used to calculate apparent optical properties of sea ice (e.g., diffuse attenuation coefficient, extinction coefficient, spectral transmittance). For these calculations, intensity fluctuations of the incident solar radiation should be corrected to make sure all the measurements of each profile are under the same incident light level. To minimize the influences of the factors mentioned above in any field measurement, the following correction sequence can be followed (Fig. 3).

(1) Correcting for the dark output. The dark output C_{D} is corrected in the corresponding spectrometer output C_{w} by subtraction, to get the signal output C_{s}. The signal output is then divided by the integration time t adopted during the spectral measurement to convert it to that at the same reference integration time of 1 s (i.e., $C_{\mathrm{s}}(\lambda,t_{1\mathrm{s}})$), facilitating the following spectral sensitivity and intensity fluctuation corrections.

(2) Acquiring and correcting for the spectral sensitivity. Spectral sensitivity is obtained using the comparison between simultaneous measurements taken by our system and the radiometer, while the radiometer output is used to indicate the spectral intensity of the solar irradiance entering the profiling system. Since the wavelengths of our system and the radiometer are not the same, linear interpolation is used to acquire the intensity of the incident solar irradiance $E_{\mathrm{R}}(\lambda)$ corresponding to each wavelength of the spectrometer based on the radiometer output $E_{\mathrm{R}}(\lambda_{\mathrm{R}})$. The spectral sensitivity $s(\lambda)$ is calculated using the interpolated solar irradiance $E_{\mathrm{R}}(\lambda)$ to divide the signal output $C_{\mathrm{s}}(\lambda,t_{1\mathrm{s}})$, which is then used to divide the measured solar irradiance profile for correcting its influence.

(3) Correcting for the immersion factor. The immersion factor of the cosine receptor is acquired experimentally in a laboratory setting following the protocols recommended by Petzold and Austin (1988). Its influence in the corrected solar irradiance profile is minimized by multiplying each of the solar irradiance collected in water by the immersion factor, wavelength by wavelength.

(4) Correcting for the intensity fluctuation of the incident light. The corrected solar irradiance profile is finally normalized for any fluctuations in the incident solar irradiance as recorded by the reference radiometer, using the radiometer output from the first measurement (i.e., that corresponding to the first irradiance measurement of one profile) as reference (Mueller et al., 2003).

3 Field examinations and derived apparent optical properties

To examine the viability and overall performance of the profiling system, this system was utilized to measure the solar irradiance distribution within different depths of sea ice in the Arctic during the 9th Chinese National Arctic Research Expedition (CHINARE) on August 12–13, 2019. The weather was cloudy, and the air temperature was approximately 1°C during these two days. The measurements were made at two blue ice floes. The first ice floe (i.e., Site 1) was located at 79.91°N, 169.13°W, with snow and ice thickness of 10 cm and 110 cm, respectively. The second ice floe (i.e., Site 2) was located at 81.15°N, 169.42°W, having a snow thickness of 5 cm and ice thickness of 114 cm.

Based on the measured solar irradiance profile the apparent optical properties of the snow/sea ice, such as the diffuse attenuation coefficient $K_{\mathrm{prof}}(\lambda)$, the extinction coefficient $K(z,\lambda)$, and the spectral transmittance $T(z,\lambda)$, could be derived. The diffuse attenuation coefficient is used to indicate the bulk attenuation rate of the light signal in sea ice/snow with depth. Given that ice/snow is horizontally homogeneous, the Beer–Lambert model could be

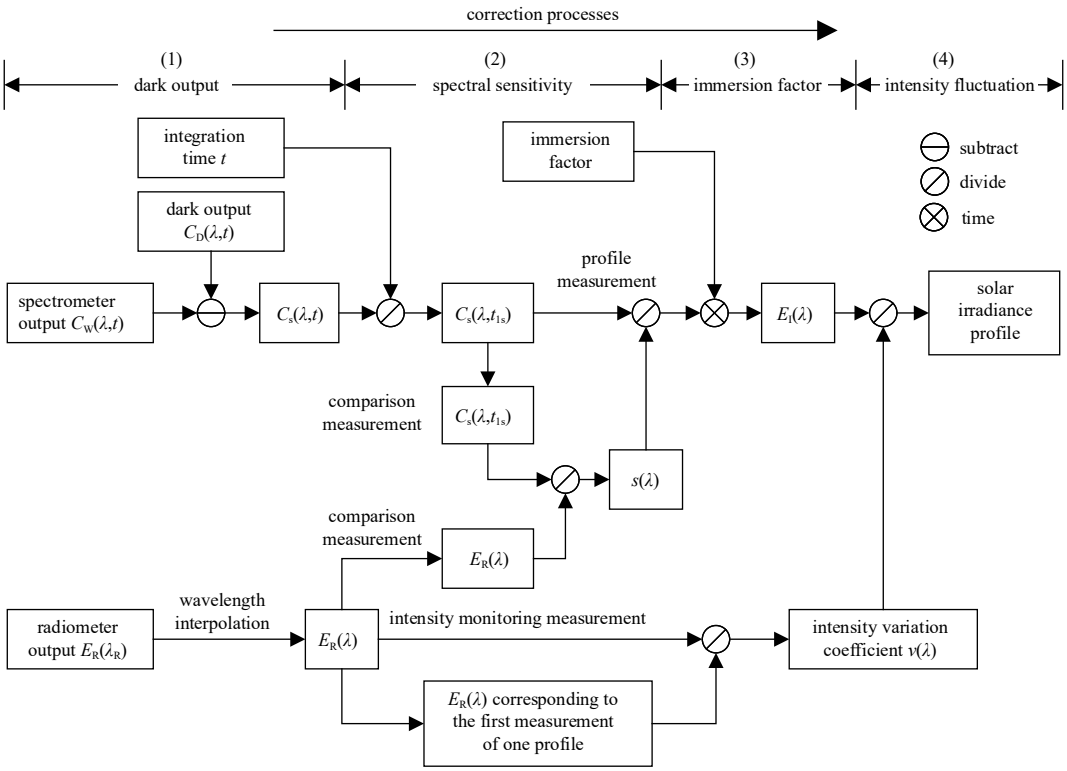

Fig. 3. Schematic of the algorithm for correcting and calibrating the spectral measurement to obtain the solar irradiance profile in sea ice.

adopted to approximate the spectral intensity of the solar irradiance $E(z,\lambda)$ at depth z as a function of the physical depth z as

$$E(z,\lambda) = E(z_0,\lambda)\, e^{-K_{prof}(\lambda)(z-z_0)}, \quad (8)$$

where z_0 and $E(z_0,\lambda)$ are the depth of the upper surface of the ice/snow in the ice floe and the corresponding solar irradiance, respectively. From Eq. (8), $K_{prof}(\lambda)$ could be inferred by

$$K_{prof}(\lambda) = -\frac{d\ln(E(z,\lambda))}{dz}. \quad (9)$$

Therefore, the diffuse attenuation coefficient $K_{prof}(\lambda)$ could be acquired by applying linear regression to the relationship between $\ln(E(z,\lambda))$ and depth z. Since most measurements of each profile were collected in ice (i.e., the amount of measurement was sufficient for linear regression), Eq. (9) was only used to calculate the diffuse attenuation coefficient of sea ice in this study. Instead, the extinction coefficient $K(z,\lambda)$ was adopted to depict the attenuation rate of the light signal in the snow with depth. It could be derived from the irradiance measurements between two depths of z_1 and z_2, following the finite-difference method:

$$K(z,\lambda) = \frac{-2}{[E(z_1,\lambda)+E(z_2,\lambda)]}\frac{E(z_2,\lambda)-E(z_1,\lambda)}{z_2-z_1}, \quad (10)$$

where $E(z_1,\lambda)$ and $E(z_2,\lambda)$ are the solar irradiance at depth of z_1 and z_2, respectively. Additionally, the spectral transmittance $T(z,\lambda)$ was also calculated by the following formula:

$$T(z,\lambda) = \frac{E(z,\lambda)}{E(0^+,\lambda)}, \quad (11)$$

where $E(0^+,\lambda)$ denotes the downwelling spectral irradiance above the snow's surface.

4 Results and discussion

From the measured profiles, we observed that the general shape of the measured solar irradiance (Figs 4b and e) was in good agreement with those measured by other commercially available oceanographic radiometers (e.g., RAMSES-ACC hyperspectral irradiance sensors) (Nicolaus et al., 2010b). This characteristic was significant not only for the measurements in the snow, but also for those in ice and water. The largest value was at about 460 nm, and it roughly decreased with the shorter and longer wavelengths. Accordingly, the effectiveness and viability of this profiling system were verified to some extent. The results also indicated that the spectral intensity of the solar irradiance decreased significantly with the depth of snow, ice, and the underlying ocean (Figs 4b and f). The rate of decrease was much higher in the snow than in ice and water, which is ascribed to the fact that the attenuation coefficient of snow is much larger than that of ice and water. Meanwhile, spectral intensity in the near-infrared region decreased much more rapidly with deeper depth than that in the visible region, as the absorption coefficient of the medium (i.e., the snow, ice and water) is much bigger in the near-infrared band than that in the visible band.

Using Eq. (10), we calculated the extinction coefficient of the snow, sea ice, and the underlying water. It denoted that spectral extinction coefficient of the snow was approximately parabolic in nature, with a minimum value of 13.30 m^{-1} at 535 nm and a mean value of 14.23 m^{-1} in the wavelength range of 350–750 nm we investigated for Site 1 (the solid line in Fig. 5a). This general relationship was also apparent for Site 2 (solid line in Fig. 5b). However, the value was much smaller with a minimum value of

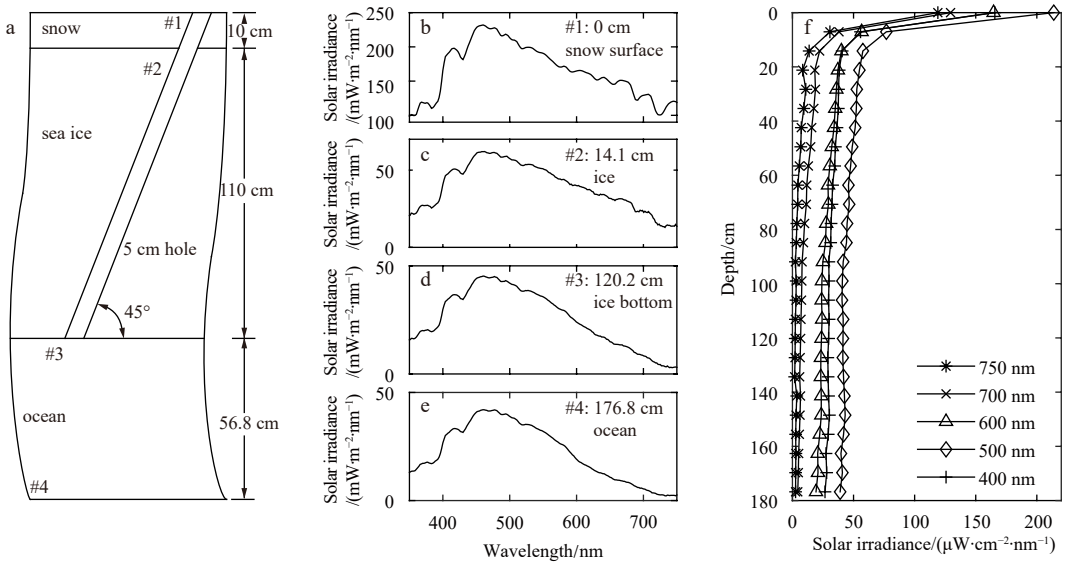

Fig. 4. Overview sketch of the irradiance profile measurements, indicating the location of four demonstrative measurements #1–#4 (a), solar irradiance as a function of wavelength for locations #1–#4 (b–e), and profiles of the solar irradiance for five selective wavelengths, extending from snow surface to the underlying ocean (f). This plot is derived from measurements collected at Site 1, which are very similar to those at Site 2.

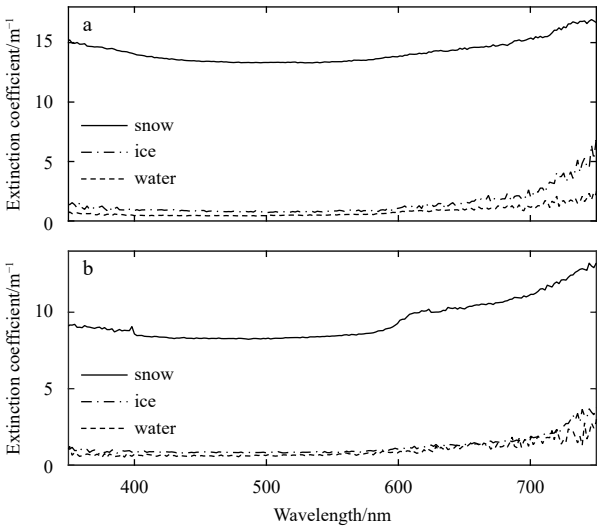

Fig. 5. Extinction coefficients of different media as a function of wavelength at Site 1 (a) and Site 2 (b).

8.34 m^{-1} at 530 nm and a mean value of 9.47 m^{-1}. The relatively small extinction coefficient of snow for Site 2 compared with Site 1 was primarily caused by the relatively thin snow that existed at Site 2 (i.e., 5 cm snow), which resulted in the influence of the 2.1 cm sea ice just below the bottom of the snow being included during the calculation of the extinction coefficient of snow. The extinction coefficient of sea ice was significant smaller than that of snow for each wavelength. Taking sea ice located in the middle of the ice column as an example, its extinction coefficient was relatively stable and changed very little for wavelengths shorter than 600 nm, having a mean value of 0.90 m^{-1} and 0.74 m^{-1} over 350–600 nm for Site 1 and Site 2 separately (dashed-dotted lines in Fig. 5). For wavelengths longer than 600 nm, the extinction coefficient increased, the rate of increase becoming larger with longer wavelengths, from 1.05 m^{-1} at 600 nm to 6.39 m^{-1} at 750 nm for Site 1, and from 0.97 m^{-1} at 600 to 3.79 m^{-1} at 750 nm for Site 2. The wavelength dependence of the underlying water was very close to that of sea ice. Shorter than 600 nm, the extinction coefficient of the water was relatively stable with a mean value of 0.50 m^{-1} and 0.66 m^{-1} for Site 1 and Site 2, respectively. Above 600 nm, it increased with longer wavelengths from 0.77 m^{-1} at 600 nm to 1.82 m^{-1} at 750 nm for Site 1, and from 0.80 m^{-1} at 600 nm to 2.81 m^{-1} at 750 nm for Site 2.

The bulk attenuation coefficient of sea ice K_{prof} was calculated using Eq. (9) and the measurements within sea ice. The results showed that the wavelength dependence of K_{prof} was similar to that of the extinction coefficient of sea ice (Figs 5 and 6). K_{prof} varied little with wavelength between 350–560 nm with a mean value of 0.25 m^{-1} and 0.31 m^{-1} for Site 1 and Site 2, respectively (Fig. 6). It increased with longer wavelengths for those longer than 560 nm, from 0.30 m^{-1} at 560 nm to 1.28 m^{-1} at 750 nm for Site 1, and from 0.33 m^{-1} at 560 nm to 2.30 m^{-1} at 750 nm for Site 2.

The spectral transmittances derived from the solar profile measurements for the two sites are shown in Fig. 7. The general wavelength dependence of the transmittance for the two measurement sites was very similar. It first increased with longer

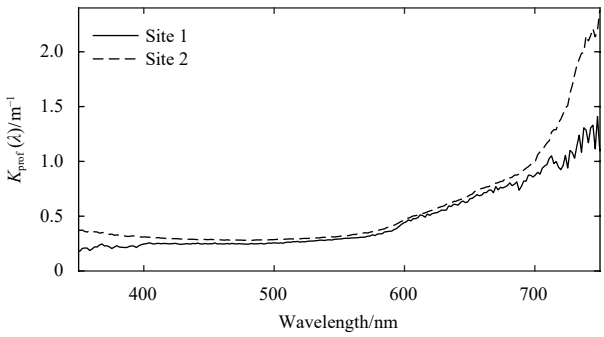

Fig. 6. Bulk attenuation coefficient of sea ice as a function of wavelength at the two measurement sites.

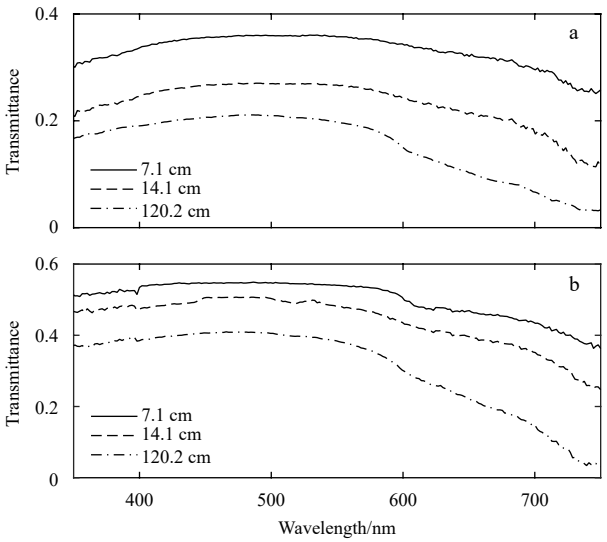

Fig. 7. Spectral transmittance of sea ice at three demonstrative depths at Site 1 (a) and Site 2 (b).

wavelengths and reached the peak point at approximately 500 nm. It then decreased with longer wavelengths, and the decreasing rate increased with longer wavelengths and deeper depths. This phenomenon is ascribed to the attenuation characteristic of sea ice medium, as shown in Figs 5 and 6. The spectral transmittance of the sea ice at each depth in Site 1 was much smaller than that in Site 2, primarily due to the much thicker snow existed in Site 1.

5 Conclusions

A new irradiance profile measurement approach and an irradiance profiling system were developed to measure the solar irradiance profile in the Arctic sea environment. The system adopted a small fiber probe which could move freely in inclined bore holes, with its optical entrance facing upward, to collect and transmit the solar irradiance signal. A miniature spectrometer was used to sense the light signal. This kind of configuration had the advantages of low self-shading, low cost and simple structure. By analyzing the processes from the light signal from entering the system to the output of the system, the input-output relationship of the system was developed. To obtain the solar irradiance profile from the system output an approach was proposed to correct the influence of the dark output of the spectrometer, the spectral sensitivity of the system, the immersion factor of the cosine receptor, and finally the intensity fluctuation of the incident light signal in the system output.

The overall performance of the profiling system was examined in summer during the 9th Chinese National Arctic Research Expedition (CHINARE) in two blue ice floes. The results indicated that the measured solar irradiance in sea ice agreed well with that obtained by other commercially available oceanographic radiometers. Meanwhile, the derived diffuse attenuation coefficient, extinction coefficient, and spectral transmittance of sea ice were comparable to those of similar sea ice measured by other optical devices. Even though the performance of the profiling system was promising, several aspects of this system might benefit from improvement. First, the spectral range of the system is limited within the visible band in the current configuration. Broadening its spectral range might help to widen the applications of the system and the measured irradiance profiles. Second, the spectral sensitivity of the system was corrected by comparative measurement. A more rigorous calibration of the spectral sensitivity by a professional calibration agency might help to improve the measurement accuracy of the system.

Acknowledgements

We thank all members of the 9th Chinese National Arctic Research Expedition (CHINARE) for their kind assistance during the examination of this system in the Arctic.

References

Arrigo K R. 2014. Sea ice ecosystems. Annual Review of Marine Science, 6: 439–467, doi: 10.1146/annurev-marine-010213-135103

Arrigo K R, Sullivan C W, Kremer J N. 1991. A bio-optical model of Antarctic sea ice. Journal of Geophysical Research: Oceans, 96(C6): 10581–10592, doi: 10.1029/91JC00455

Arrigo K R, van Dijken G, Pabi S. 2008. Impact of a shrinking Arctic ice cover on marine primary production. Geophysical Research Letters, 35(19): L19603, doi: 10.1029/2008GL035028

Ehn J K, Mundy C J, Barber D G. 2008a. Bio-optical and structural properties inferred from irradiance measurements within the bottommost layers in an Arctic landfast sea ice cover. Journal of Geophysical Research: Oceans, 113(C3): C03S03, doi: 10.1029/2007JC004194

Ehn J K, Papakyriakou T N, Barber D G. 2008b. Inference of optical properties from radiation profiles within melting Landfast sea ice. Journal of Geophysical Research: Oceans, 113(C9): C09024, doi: 10.1029/2007JC004656

Feister U, Grewe R. 1995. Spectral albedo measurements in the UV and visible region over different types of surfaces. Photochemistry and Photobiology, 62(4): 736–744, doi: 10.1111/j.1751-1097.1995.tb08723.x

Frey K E, Perovich D K, Light B. 2011. The spatial distribution of solar radiation under a melting Arctic sea ice cover. Geophysical Research Letters, 38(22): L22501, doi: 10.1029/2011GL049421

Grenfell T C, Light B, Perovich D K. 2006. Spectral transmission and implications for the partitioning of shortwave radiation in arctic sea ice. Annals of Glaciology, 44: 1–6, doi: 10.3189/172756406781811763

Grenfell T C, Maykut G A. 1977. The optical properties of ice and snow in the Arctic Basin. Journal of Glaciology, 18(80): 445–463, doi: 10.1017/S0022143000021122

Grenfell T C, Perovich D K. 1984. Spectral albedos of sea ice and incident solar irradiance in the southern Beaufort Sea. Journal of Geophysical Research: Oceans, 89(C3): 3573–3580, doi: 10.1029/JC089iC03p03573

Haas C, Thomas D N, Bareiss J. 2001. Surface properties and processes of perennial Antarctic sea ice in summer. Journal of Glaciology, 47(159): 613–625, doi: 10.3189/172756501781831864

Lei Ruibo, Zhang Zhanhai, Matero I, et al. 2012. Reflection and transmission of irradiance by snow and sea ice in the central Arctic Ocean in summer 2010. Polar Research, 31(1): 17325, doi: 10.3402/polar.v31i0.17325

Leu E, Mundy C J, Assmy P, et al. 2015. Arctic spring awakening-Steering principles behind the phenology of vernal ice algal blooms. Progress in Oceanography, 139: 151–170, doi: 10.1016/j.pocean.2015.07.012

Light B, Grenfell T C, Perovich D K. 2008. Transmission and absorption of solar radiation by Arctic sea ice during the melt season. Journal of Geophysical Research: Oceans, 113(C3): C03023, doi: 10.1029/2006jc003977

Light B, Perovich D K, Webster M A, et al. 2015. Optical properties of melting first-year Arctic sea ice. Journal of Geophysical Research: Oceans, 120(11): 7657–7675, doi: 10.1002/2015JC011163

Maslanik J A, Fowler C, Stroeve J, et al. 2007. A younger, thinner Arctic ice cover: Increased potential for rapid, extensive sea-ice loss. Geophysical Research Letters, 34(24): L24501, doi: 10.1029/2007GL032043

Mueller J L, Morel A, Frouin R, et al. 2003. Radiometric measurements and data analysis protocols. In: Mueller J L, Fargion G S,

Mcdain C R, eds. Ocean Optics Protocols for Satellite Ocean Color Sensor Validation, Revision 4, Volume III. Greenbelt, Maryland, USA: Goddard Space Flight Space Center, NASA/TM-2003-211621/Rev-Vol III

Nan Liwen, Wang Hangzhou, Han Jiwan, et al. 2017. Development and evaluation of a driver circuitry for miniature spectrometers used in cold environments. IEICE Electronics Express, 14(20): 20170876, doi: 10.1587/elex.14.20170876

Nicolaus M, Gerland S, Hudson S R, et al. 2010a. Seasonality of spectral albedo and transmittance as observed in the Arctic Transpolar Drift in 2007. Journal of Geophysical Research: Oceans, 115(C11): C11011, doi: 10.1029/2009jc006074

Nicolaus M, Hudson S R, Gerland S, et al. 2010b. A modern concept for autonomous and continuous measurements of spectral albedo and transmittance of sea ice. Cold Regions Science and Technology, 62(1): 14–28, doi: 10.1016/j.coldregions.2010.03.001

Petzold T, Austin R W. 1988. Characterization of MER-1032. San Diego: University of California

Saenz B T, Arrigo K R. 2012. Simulation of a sea ice ecosystem using a hybrid model for slush layer desalination. Journal of Geophysical Research: Oceans, 117(C5): C05007, doi: 10.1029/2011JC007544

Serreze M C, Holland M M, Stroeve J. 2007. Perspectives on the Arctic's shrinking sea-ice cover. Science, 315(5818): 1533–1536, doi: 10.1126/science.1139426

Thomas D N, Dieckmann G S. 2009. Sea Ice. 2nd ed. West Sussex: John Wiley and Sons

Vancoppenolle M, Meiners K M, Michel C, et al. 2013. Role of sea ice in global biogeochemical cycles: Emerging views and challenges. Quaternary Science Reviews, 79: 207–230, doi: 10.1016/j.quascirev.2013.04.011

Wang Hangzhou, Nan Liwen, Huang Hui, et al. 2017. Adaptive measurement method for miniature spectrometers used in cold environments. Applied Optics, 56(28): 8029–8039, doi: 10.1364/AO.56.008029

Wang Hangzhou, Song Hong, Chen Ying, et al. 2015. Correcting temperature dependence in miniature spectrometers used in cold polar environments. Applied Optics, 54(11): 3162–3172, doi: 10.1364/AO.54.003162

Xu Zhantang, Yang Yuezhong, Sun Zhaohua, et al. 2012. In situ measurement of the solar radiance distribution within sea ice in Liaodong Bay, China. Cold Regions Science and Technology, 71: 23–33, doi: 10.1016/j.coldregions.2011.10.005

Zhao Jinping, Li Tao. 2009. The solar radiation penetrating sea ice with very low solar altitude. Periodical of Ocean University of China (in Chinese), 39(5): 822–828